OPEN ACCESS



Detection of Rydberg Lines from the Atmosphere of Betelgeuse

W. R. F. Dent , G. M. Harper , A. M. S. Richards , P. Kervella , and L. D. Matthews L. D. Matthews , and L. D. Matthews Cordova 3107, Vitacura, Casilla 763 0355, Santiago, Chile Center for Astrophysics and Space Astronomy, University of Colorado Boulder, USA Jodrell Bank Centre for Astrophysics, Department of Physics and Astronomy, The University of Manchester, Manchester M13 9PL, UK LESIA, Observatoire de Paris, Université PSL, CNRS, Sorbonne Université, Université Paris-Cité, 5 Place Jules Janssen, 92195 Meudon, France Massachusetts Institute of Technology Haystack Observatory, 99 Millstone Road, Westford, MA 01886, USA Received 2024 March 20; revised 2024 April 3; accepted 2024 April 4; published 2024 April 25

Abstract

Emission lines from Rydberg transitions are detected for the first time from a region close to the surface of Betelgeuse. The H30 α line is observed at 231.905 GHz, with an FWHM \sim 42 km s⁻¹ and extended wings. A second line at 232.025 GHz (FWHM \sim 21 km s⁻¹), is modeled as a combination of Rydberg transitions of abundant low first ionization potential metals. Both H30 α and the Rydberg combined line X30 α are fitted by Voigt profiles, and collisional broadening with electrons may be partly responsible for the Lorentzian contribution, indicating electron densities of a few 10⁸ cm⁻³. X30 α is located in a relatively smooth ring at a projected radius of 0.9× the optical photospheric radius R_{\star} , whereas H30 α is more clumpy, reaching a peak at \sim 1.4 R_{\star} . We use a semiempirical thermodynamic atmospheric model of Betelgeuse to compute the 232 GHz (1.29 mm) continuum and line profiles making simple assumptions. Photoionized abundant metals dominate the electron density, and the predicted surface of continuum optical depth unity at 232 GHz occurs at \sim 1.3 R_{\star} , in good agreement with observations. Assuming a Saha–Boltzmann distribution for the level populations of Mg, Si, and Fe, the model predicts that the X30 α emission arises in a region of radially increasing temperature and turbulence. Inclusion of ionized C and non-LTE effects could modify the integrated fluxes and location of emission. These simulations confirm the identity of the Rydberg transition lines observed toward Betelgeuse and reveal that such diagnostics can improve future atmospheric models.

Unified Astronomy Thesaurus concepts: Red supergiant stars (1375); Stellar atmospheres (1584); Radio interferometry (1346)

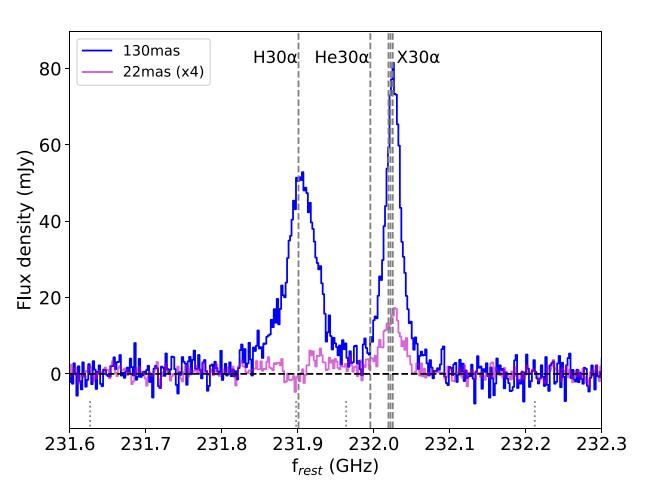
1. Introduction

Red supergiants (RSGs) are an important late stage in the evolution of massive stars. Their high mass-loss rates are one of the major sources of enrichment of the interstellar medium, yet the details of the mass-loss mechanism are not fully understood. Interaction of granulation, convective cells, and pulsations with magnetic fields, in addition to scattering by lines or nascent dust followed by radiation pressure, are mechanisms proposed to initiate mass loss and drive the wind (Airapetian et al. 2000; Verhoelst et al. 2009; Arroyo-Torres et al. 2015; Decin 2021). Episodic and inhomogeneous ejection may also play a significant role (Montargès et al. 2021; Humphreys & Jones 2022). High-resolution infrared and millimeter observations of the closest RSGs show molecular gas-mostly observed through CO, SiO, and H2O-lying in a highly clumped shell (or MOLsphere) at radii of $\sim 1.5 R_{\star}$ (Perrin et al. 2007). Radio through millimeter continuum spectral energy distributions show optically thick free-free emission arising from a hot chromosphere with a small filling factor embedded in more pervasive lukewarm plasma heated to 2000–3600 K, and this extends from 1.3 R_{\star} out to tens of stellar radii at the longer (centimeter) wavelengths (Lim et al. 1998; O'Gorman et al. 2020). How the clumpy MOLsphere and the chromosphere are related and involved in the mass loss from these stars remains unclear.

Original content from this work may be used under the terms of the Creative Commons Attribution 4.0 licence. Any further distribution of this work must maintain attribution to the author(s) and the title of the work, journal citation and DOI.

At a distance of 222 pc (Harper et al. 2017a), Betelgeuse is the second-closest RSG after Antares and consequently has been extensively studied as an archetype (e.g., Wheeler & Chatzopoulos 2023). Its K-band (2.2 μ m) spectro-interferometric angular diameter of 42.5 mas (Ohnaka et al. 2011) makes it resolvable with current IR and radio instruments. Harper et al. (2017b) found Betelgeuse's center-of-mass radial velocity to be $V_{\rm helio} = (20.9 \pm 0.3) \; {\rm km \, s}^{-1} \; {\rm based on a mean of}$ four different diagnostics, and Kervella et al. (2018) measured $V_{\rm helio} = (20.4 \pm 0.1) \; {\rm km \, s}^{-1} \; {\rm from \; Atacama \; Large \; Millimeter} /$ submillimeter Array (ALMA) SiO emission. We adopt V_{\star} = $V_{\text{helio}} = 20.9 \text{ km s}^{-1}$ (corresponding to V_{lsr} of 4.9 km s⁻¹) and $R_* = 1014 \ R_{\odot}$. The structure is not symmetrical—continuum hot spots in radio through millimeter and infrared continuum are seen on scales of hundreds down to \sim 15 mas (Haubois et al. 2009; Richards et al. 2013; O'Gorman et al. 2020), and macroscopic gas motions have been imaged in the clumpy gas on scales down to tens of mas—within 0.5 R_{\star} of the photosphere (e.g., Montargès et al. 2014; Kervella et al. 2018). In 2020, Betelgeuse underwent a historically significant 1.7 mag drop in V-band brightness, ascribed either to ejection of an obscuring dust clump along the line of sight or the formation of cool regions on the photosphere correlated with the pulsating atmosphere or both (Harper et al. 2020; Montargès et al. 2021). This has stirred up considerable new interest in this star.

Rydberg transition lines (RTLs) of hydrogen result from changes in the principal quantum number n. In addition to H and He, RTLs of heavier elements such as C, Si, etc. have also been observed, but because such atoms with electrons in high-energy



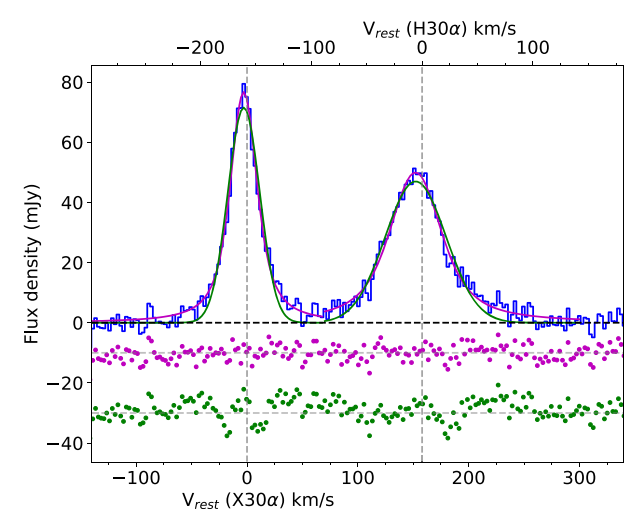


Figure 1. Spectrum of 30α Rydberg lines from Betelgeuse. Left panel shows emission after continuum subtraction, integrated over a 130 mas aperture (blue) and from only the central 22 mas (scaled by $\times 4$, magenta). The frequencies of $H30\alpha$, $He30\alpha$, and the group of O, Mg, S, and Fe (in order of increasing Rydberg frequency and marked $X30\alpha$) are indicated by the vertical dashed lines. Also shown by short dotted lines are the line frequencies of $H30\alpha$. Right panel shows the spectrum after binning by two channels, on velocity scales based on the calculated $H30\alpha$ and $H30\alpha$ rest frequencies in Table 1. Voigt profiles (magenta lines) provide good fits to the line core and wings, while Gaussian profiles (green) underpredict the line wings. Residuals for the two types of profiles are shown offset below. Details of the fits are given in Table 1. Axes in both cases are adjusted to the rest frame with respect to V_{\star} .

levels are hydrogenic, their lines appear close in frequency. In environments such as HII regions, planetary nebulae, photodissociation regions, and young stellar objects, Rydberg transitions result from radiative recombination of the ions, and Gordon & Sorochenko (2002) provide an extensive review of the resulting radio recombination lines. Olofsson et al. (2021) recognized that the emission around 232.02 GHz in the binary AGB star HD101584 is likely due to a superposition of 30α RTLs from elements heavier than C, for which they coined the term $X30\alpha$. Their model indicated that Mg30 α may dominate and, moreover, the environment is such that these lines may not be solely due to radiative recombination (hence the more general term RTL). Infrared RTLs from Mg I as high as n = 8 have also been observed and modeled in the Sun (Chang et al. 1991; Carlsson et al. 1992) and cool evolved stars (Uitenbroek & Noyes 1996; Sundqvist et al. 2008).

In this work, we present the first detection of RTLs in the atmosphere of Betelgeuse, at \sim 232 GHz, using ALMA. These observations were obtained as part of a multiband high-resolution program to study this star after the Great Dimming event, providing images of the continuum and a number of molecular lines. Full results will be presented in a separate paper.

2. Observations

Betelgeuse was observed using ALMA in its most extended configuration giving a maximum baseline of 15 km, in two executions on 2023 August 3 and 27. We used a total bandwidth of 7.5 GHz in four spectral windows centered at 214.769, 217.073, 220.266 and 231.966 GHz (1.40–1.29 mm) with a spectral channel spacing of 0.976 MHz and an effective spectral resolution of 2.6 km s⁻¹ at 232 GHz after Hanning smoothing. Standard phase referencing was used, cycling to the phase calibrator J0552+0313 (at 4°.2 separation) every 80–90 s. The bandpass was calibrated using J0510+1800. The standard calibrated measurement sets (visibility data) from the ALMA CASA pipeline were concatenated, and the line-free channels were used made a continuum image, which provided a model for phase self-calibration in CASA (CASA Team et al. 2022).

The final continuum image was made solving for the stellar spectral index, using a restoring beam of (27×19) mas FWHM at PA 51° and achieving an off-source continuum noise level of 0.024 mJy beam⁻¹. The calibration was applied to all spectral channels, and we made spectral image cubes before and after continuum subtraction. The restoring beam at around 232 GHz is (28.8×20.6) mas FWHM at PA 50°, and the noise level per spectral channel is $\sigma_{\rm rms} = 0.9$ mJy beam⁻¹. The maximum recoverable scale is 0."35. The flux scale is accurate to \sim 7%, and the astrometric accuracy is \sim 3 mas.

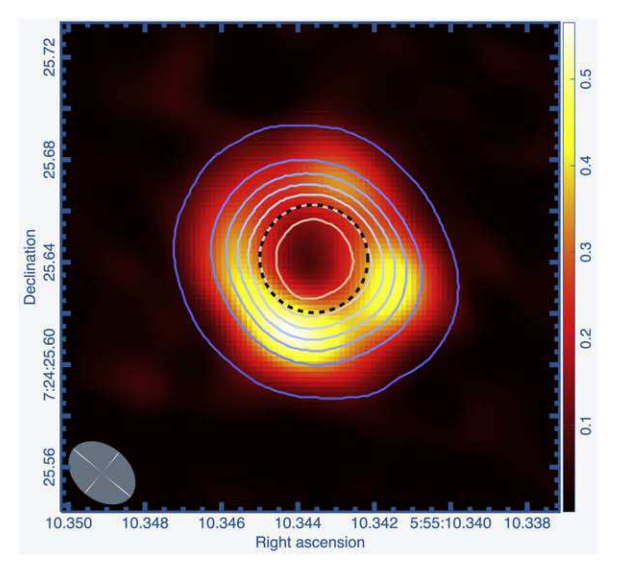
3. Results

The ALMA resolution around 232 GHz provides \sim two resolution elements across the photosphere, and a 2D Gaussian component fitted to the 214–233 GHz continuum has a radius at FWHM (after deconvolution from the beam) of $R_{232\rm GHz}=30$ mas. We measure the stellar center as ICRS 05:55:10.3435 \pm 07:24:25.640 with \sim 3 mas stochastic uncertainty. In the image plane (convolved with the beam) we found that an aperture of radius 65 mas (R_{65}) enclosed all the emissions, both line and continuum. The disk-average spectral index between 214 and 233 GHz (α) is approximately 1.7, and the continuum flux density around 232 GHz is 297 \pm 20 mJy in R_{65} .

A number of lines of SiO and CO are covered by this project—these will be discussed in a later paper—but here we focus on two bright emission lines found around 232 GHz, which we identify as 30α Rydberg transitions.

Figure 1 (left panel) shows the continuum-subtracted integrated spectrum taken within R_{65} . Frequencies are shown in the stellar rest frame, and the rest frequencies of some 30α RTLs are indicated. We also show TiO_2 frequencies covered by this spectrum, as this molecule has been detected in some other RSGs (e.g., De Beck et al. 2015). However, based on the relative CDMS/JPL intensities listed in Splatalogue, the most prominent TiO_2 lines should be at 231.626 and 231.963 GHz, and we conclude that there is no evidence of significant contribution

https://splatalogue.online/



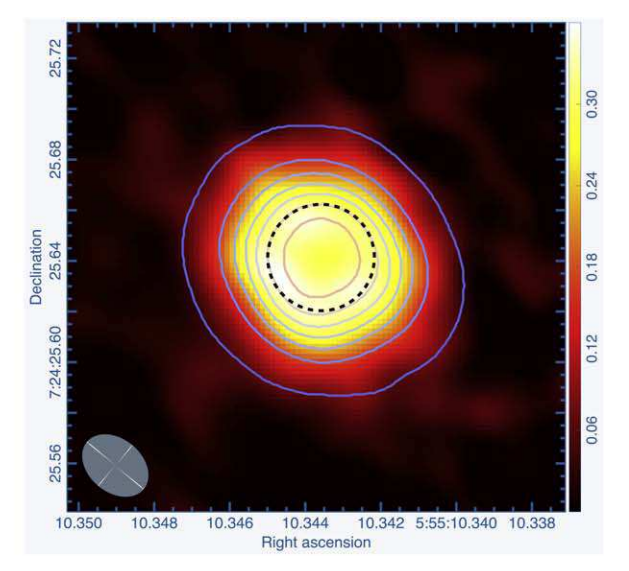


Figure 2. Maps of the continuum-subtracted integrated emission of H30 α (231.82–231.97 GHz, left) and X30 α (231.97–232.08 GHz, right) in the vicinity of Betelgeuse. The size of the IR photosphere is shown by the dashed circle, and the 214–233 GHz continuum is shown by the contours. Contours start at 1 mJy beam⁻¹, with an interval of 8 mJy beam⁻¹, and the color scales of line intensity are in Jy beam⁻¹ km s⁻¹. The beam size is shown lower left.

Table 1
Line Characteristics

Line	Calculated Freq. (GHz)	Measured Freq. (GHz) ^a	Freq. err. (GHz) ^b	Width (FWHM) (km s ⁻¹) ^c	FWZM (km s ⁻¹) ^d	Peak Line Flux (mJy) ^e	Total Intensity (Wm ⁻²) ^e	Radius (mas) ^f
$H30\alpha$	231.9009 ^g	231.9055	0.0004	42.6 (31.0,19.4)	180	50.6	4.5×10^{-19}	28
$X30\alpha$	232.0232 ^h	232.0255	0.0002	21.5 (15.3,10.2)	120	80.8	5.7×10^{-19}	18
${ m He}30\alpha$	231.9954 ^g		•••	•••	•••	<5		•••

Notes.

from this species. No other obvious candidates for these lines could be found. The characteristics of the observed lines and comparison with expected line frequencies are given in Table 1, including an upper limit for the He30 α line. The brightest peak is centered close to the cluster of 30α RTLs from high-abundance elements including Mg, Si, Fe, and perhaps O and S. This is similar to the cluster of lines noted by Olofsson et al. (2021) in HD101584. The left panel in Figure 1 illustrates the frequencies of these elements based on the Rydberg formula (Towle et al. 1996). The center frequency of this cluster is affected by the weighting by the fine-structure lines as well as the relative contributions from the different elements and is discussed further in Section 4. Although the clustering of lines from the heavier elements make it difficult to separate the dominant species in the $X30\alpha$ group, the emission peaks of both the H30 α and X30 α lines appear to be blueshifted relative to V_{\star} , by -5.9 and -3.0 km s⁻¹ respectively; possible explanations for this will also be discussed in Section 4. Also shown in Figure 1 (left panel) is the integrated spectrum of only the central 11 mas radius, R_{11} , covering approximately the central beam on the photosphere. Here the $H30\alpha$ line shows a clear dip slightly below the continuum level, indicating

absorption centered at \sim 231.898 GHz. This is \sim 10 km s⁻¹ redshifted with respect to the overall emission, with the absorption profile appearing narrower than the main emission component. These observations suggest variations in the gas radial motion and line broadening along the line of sight.

The line width of $H30\alpha$ is approximately 2 times broader than $X30\alpha$. Although there is some contribution to the $X30\alpha$ width from the potential multiple atomic components, Figure 1 shows that this is relatively small compared with the observed line width. Both $H30\alpha$ and $X30\alpha$ have broad wings and were better fitted by Voigt rather than Gaussian profiles. This is illustrated in the right panel of Figure 1, and the fitted widths (FWHM) of the Gaussian component in both cases was $\sim 3/2$ of the Lorentzian (Table 1). By comparison, the absorption and emission profiles of SiO have line widths of typically $\sim 20~{\rm km~s^{-1}}$ FWHM (Kervella et al. 2018), and optical lines can range from 15 km s⁻¹ up to $\sim 40~{\rm km~s^{-1}}$ in the upper photosphere (Jadlovský et al. 2023).

Figure 2 compares the angular distribution of the two RTLs and 1.3 mm stellar continuum emission across Betelgeuse, and the left panel of Figure 3 shows the projected radial distributions. The RTLs are generally more extended than the stellar

^a Fitted center frequency in target frame adjusted to $V_{\star} = V_{\text{helio}}$ of 20.9 km s⁻¹.

^b Formal fitting error.

^c Combined FWHM, fitted using a Voigt profile (FWHM of individual Gaussian and Lorentzian components are given in brackets)

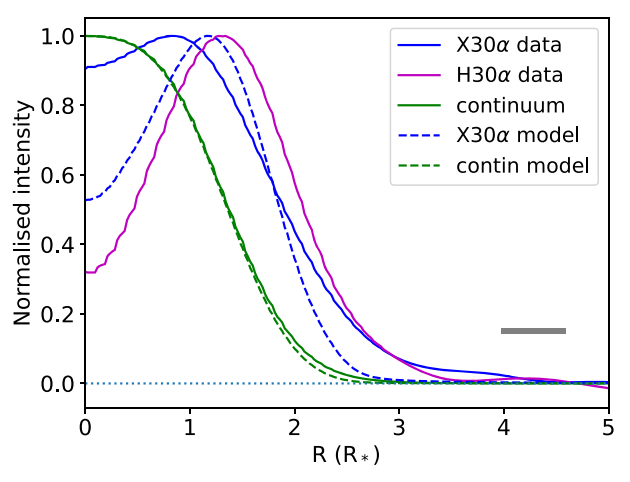
^d Full width at approximate noise level, estimated from spectra.

^e In aperture of 130 mas diameter.

f Projected radius of peak emission, azimuthally averaged.

g Rest frequency from Rydberg formula (Towle et al. 1996).

h Combined center rest frequency (see Section 4).



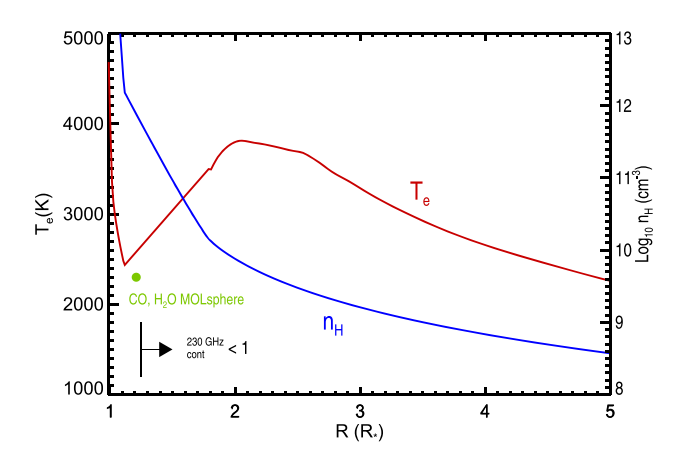


Figure 3. Azimuthally averaged projected radial distributions. Left panel shows the RTLs (blue and magenta) and the 1.3 mm continuum (green). Solid lines are the observations, and dashed lines represent the model convolved with the azimuthally averaged ALMA beam (size shown lower right). Right panel illustrates the adopted semiempirical model structure, including the radial profile of the gas (electron) temperature T_e and neutral H density n_H above the photosphere. Also shown are the inner edge of the MOLsphere and the $\tau = 1$ continuum radius at the observing frequency. The electron density (not shown) is dominated by the photoionization of abundant low FIP elements, Mg, Si, and Fe, with contributions from C and S.

continuum and lies in ring-like structures of radii 1.4 and $0.9\,R_\star$, resembling the molecular shell observed by Kervella et al. (2018) in SiO and CO lines. The molecular shell has a somewhat larger radius ($\sim 2\,R_\star$) although this may partly be affected by blending with the line absorption against the stellar photosphere. One characteristic of both RTL images is the central dip toward the photosphere. This is particularly prominent in $H30\alpha$, but in this case it is partly generated by the narrow dip in the central line profile—which is thought to be due to absorption against the bright stellar continuum (left panel in Figure 1). Note that these are continuum-subtracted line maps, and the lines are mostly seen in emission against a bright optically thick continuum background. The temperature in the model increases with radius in the emitting region (Figure 3), which in this case results in the lines being in emission.

 $X30\alpha$ emission has more symmetric, less clumpy structure than either $H30\alpha$ or published SiO maps: azimuthal variations of $\sim 10\%$ are found in the $X30\alpha$ map (Figure 2), which compares with the variations of a factor of two or more in the $H30\alpha$ clumps and in other lines (Kervella et al. 2018). This—and the different radial profiles in Figure 3—indicate that the $X30\alpha$ emission is not arising from the same region as the $H30\alpha$. Closer examination of both data cubes shows no significant velocity differences between the emission clumps in Figure 2; also the integrated line profiles are rather smooth and symmetrical. These characteristics suggest that the RTLs are not strongly masering although weak amplification of the continuum may still be occurring (see Section 4).

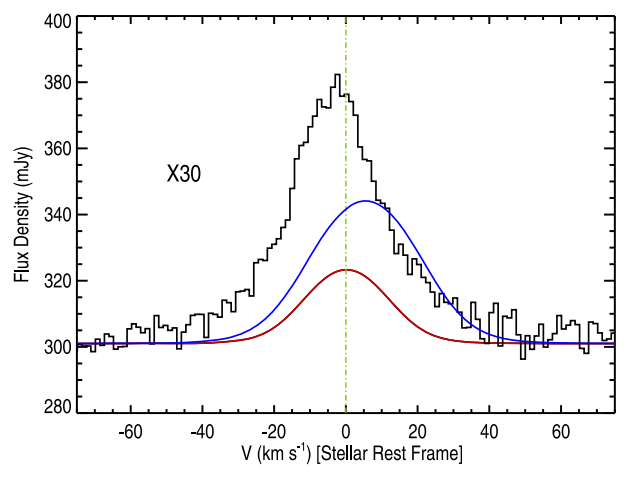
4. Models and Discussion

RTL α lines are formed by dipole transitions between $\Delta n = 1$ energy levels that are strongly collisionally coupled with the next ionization state, so their emission strength depends on the abundance of that state.

To examine whether the putative 232 GHz Rydberg transitions are consistent with atmospheric conditions surrounding Betelgeuse, we computed $\rm H30\alpha$ and $\rm X30\alpha$ line profiles using a semiempirical thermodynamic atmospheric model. We have used an update of the model of Harper et al. (2001) to include the revised distance and photospheric Rosseland angular diameter. It uses the run of hydrogen ($n_{\rm H}$) and electron ($n_{\rm e}$)

densities and the mean electron temperature (T_e) with stellar radius derived from the Very Large Array radio continuum visibilities from Lim et al. (1998), a compilation of published radio and millimeter-radio fluxes (Harper et al. 2001), and Hubble Space Telescope ultraviolet (UV) fluxes (Carpenter et al. 1994). This model represents the mean 1D dominant lukewarm chromosphere and not the small filling factor of hot chromospheric plasma that gives rise to the rich UV spectrum. It also does not include pockets of cold molecular material. The outer reaches of the 2001 model were scaled to the new distance as described in Harper et al. (2009, Section B1), and the inner region now includes a spherical MARCS photospheric model with $T_{\rm eff} = 3650$ and $\log g_{\star} = -0.5$ (Gustafsson et al. 2008) with a turbulently extended chromospheric region. Full details of the revised semiempirical model will be published elsewhere, but the radial dependence of $n_{\rm H}$ (which is predominantly neutral) and $T_{\rm e}$ are shown in the right panel of Figure 3.

The electron density in the RTL-forming region in the lower chromosphere is dominated by photoionized abundant low first ionization potential (FIP) metals, namely Mg, Fe, and Si. The intense chromospheric UV radiation field that arises from the pervasive, small filling factor of hot plasma can ionize the low FIP elements and potentially some S and C but not O, whose ionization is tightly coupled to neutral H by charge exchange (Judge 1986, and references therein). In the chromosphere, molecular hydrogen will have a negligible abundance. In the extended atmosphere to a first approximation, if Mg, Fe, Si are ionized, then $n_{\rm e} \simeq 10^{-4} n_{\rm H}$, and if C and S are fully ionized, then $n_{\rm e} \simeq 3 \times 10^{-4} n_{\rm H}$. To examine the RTLs observed both on and off the 232 GHz stellar disk, it was assumed the upper and lower levels are hydrogenic and populated in their Boltzmann ratios. The absolute level populations are derived from the Saha-Boltzmann equation from the atmospheric hydrogen and electron densities. We adopt the Fe and C abundances from Carr et al. (2000) with the isotopic ratio $^{12}\text{C}/^{13}\text{C} = 6$ from Lambert et al. (1984) and the Si abundance and isotopic ratios given in Ohnaka (2014). Solar abundances (Asplund et al. 2021) were adopted for Mg and S, and otherwise isotopic terrestrial isotropic ratios were used.



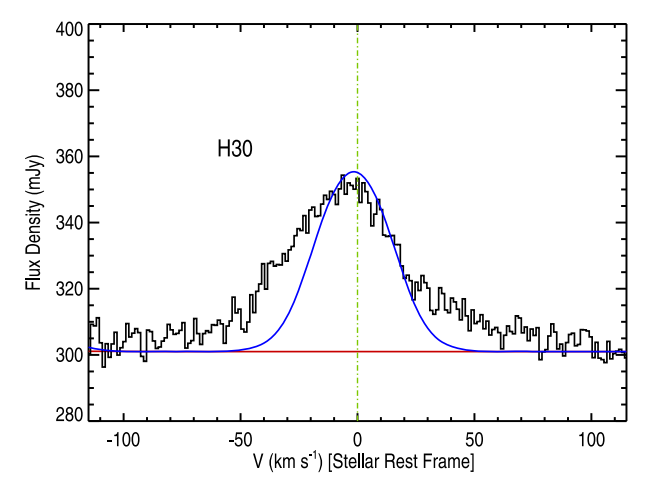


Figure 4. Simulations of the RTLs computed with and without enhanced C and H ionization. Left: $X30\alpha$ (232.023 GHz). Mg, Si, and Fe computed with the Saha–Boltzmann-level populations producing $\sim 1/4$ of the observed flux (shown by the red line). In the second simulation (blue) the C is singly ionized, and this improves the match of the total fluxes but shifts the combined profile redward by ~ 5 km s⁻¹, farther away from the observed peak. Right: H30 α (231.901 GHz). In the first simulation no emission is predicted (see Section 4 for details). We artificially increased the ionization fraction of H to 1×10^{-4} , which now leads to H30 α emission. Inclusion of non-LTE level populations will likely alter the predicted line fluxes. The observed lines, especially H30 α , show excess flux in the line wings.

We computed the $X30\alpha$ cluster line profile with the following species $^{12}\text{C}, \,^{13}\text{C}, \,^{23}\text{Na}, \,^{24}\text{Mg}, \,^{25}\text{Mg}, \,^{26}\text{Mg}, \,^{28}\text{Si}, \,^{29}\text{Si}, \,^{30}\text{Si}, \,^{32}\text{S},$ and ^{56}Fe , in addition to H30 α . The semiempirical atmospheric model is based on continuum data and is agnostic to atmospheric velocity fields, so we assume isotropic nonthermal motions ramping from $11\,\mathrm{km\,s^{-1}}$ at $1.3\,R_{\star}$ to $23\,\mathrm{km\,s^{-1}}$ at $2.0\,R_{\star}$ (FWHM), consistent with the observed widths of narrow (low-opacity) far-ultraviolet emission lines (Carpenter et al. 2018). The Doppler velocity in each line profile is the thermal motion added in quadrature to the nonthermal motion. The rest frequencies were initially taken to be purely hydrogenic (see Towle et al. 1996). The continuum opacity sources included were H free–free, H $^-$ free–free, and metal $^-$ free–free. The spherical radiative transfer problem, a class of local thermodynamic equilibrium (LTE) but with non-LTE ionization balances, was solved for the line and continuum.

In the continuum, the radial optical depth $\tau_{232\,\mathrm{GHz}} = 1$ occurs near $1.3\,R_{\star}$, i.e., above the photosphere, and the $\mathrm{X}30\alpha$ Rydberg emission occurs above this radius in the region where the gas temperature and turbulence are increasing outwards. The 232 GHz stellar continuum flux density was computed to be $\simeq 300$ mJy, in good agreement with the observed value. The left panel of Figure 3 shows the computed disk size convolved with the ALMA beam (green dashed line), also in good agreement with that observed (solid green), indicating that this is a reasonable model to compute the RTLs to establish their likelihood in Betelgeuse.

A comparison of the observed and model spectra is shown in Figure 4. The left panel shows the computed $X30\alpha$ spectrum (red) where the electrons come from Mg, Si, and Fe and is plotted with respect to their abundance-weighted hydrogenic rest frequency (232.0232 GHz) in the rest frame of the star. A second simulation (blue) with fully ionized C and S still underestimates the observed flux but shifts the overall line profile redward by $\sim 5 \, \mathrm{km \, s^{-1}}$ (away from the observed rest frequency) owing to the lower-C atomic mass. In the right panel no hydrogen emission is produced in this model, as expected (see below); however, the addition of a small hydrogen ionization fraction (1×10^{-4}) leads to $H30\alpha$ emission at its rest velocity, shown by the blue curve.

We choose not to overinterpret the computed line fluxes because we have ignored non-LTE level population effects that are likely to change opacities and source functions and alter the distribution of the emission. For example, collisional and radiative cascades from higher n levels and Mg II, and photoexcitation from the chromosphere and star need to be included to accurately predict the non-LTE level populations. This might explain why the predicted $X30\alpha$ spatial distribution of the emission shown in Figure 3 is more extended than the observations. We have explored schematic non-LTE simulations and find that masering is possible against the stellar disk and non-LTE effects are likely. To investigate the uncertainty of the $X30\alpha$ rest frequencies, we computed an 1-state-resolved hydrogenic Einstein A-value weighted frequency for ²⁴Mg using the energy-level expressions in Chang (1987). This revealed a blueshifted frequency, and presumably similar $\sim 1 \text{ km s}^{-1}$ uncertainties exist for the more complex Si and Fe atoms.

Both the $X30\alpha$ and $H30\alpha$ lines appear blueshifted with respect to the model spectra, by 3 and 6 km s⁻¹ respectively. While the on-disk profile can easily be affected by inward and/ or outward bulk motions, the annular emission that samples the volume of atmosphere both in front of and behind the star should be less affected. The ALMA emission shows no significant difference in the velocity centroid in the annular region. Although there is some uncertainty in the $X30\alpha$ central rest frequency (see previous paragraph), the $H30\alpha$ line has an essentially exact rest frequency, and its off-disk spectrum is also blueshifted. One possibility is some mild maser amplification of the stellar background continuum, along with net outward motion along the line of sight; this could also explain why the $X30\alpha$ line emission is more compact than predicted (see Figure 3). Further exploration of these line shifts and structure at higher spatial resolution and in different transitions would help elucidate these differences.

The synthetic line profiles broadened by turbulence are similar to first order to those observed but lack the extended wings. Additional sources of line width have been discussed by Olofsson et al. (2021); one possibility is collisional broadening —with electrons, ions or neutrals. The mean electron density measured from the n_e -sensitive C II] 2325 Å emission multiplet

in the hot chromospheric component is $\simeq 2 \times 10^8 \, \mathrm{cm}^{-3}$ (Judge & Carpenter 1998), and Harper & Brown (2006) show that the local density may reach $10^9 \, \mathrm{cm}^{-3}$. Assuming the approximation from Brocklehurst & Seaton (1972, Equation (4.8)) is applicable to 30α transitions, using $T_e = 3000 \, \mathrm{K}$ in the emitting region from the model in Figure 3, the observed Lorentzian component of $H30\alpha$ in Table 1 would indicate an electron density of $\sim 3 \times 10^8 \, \mathrm{cm}^{-3}$. Because of the strong dependence on the Rydberg transition, measurements of the widths of other lines would be of interest to confirm this mechanism. Betelgeuse's measured surface longitudinal magnetic field is $\sim 1 \, \mathrm{G}$ (Aurière et al. 2010), which is insufficient to induce significant Zeeman broadening.

We do not expect hydrogen to have any noticeable ionization in the lukewarm chromosphere, but it is very sensitive to small amounts of embedded hot plasma such as that which excites the UV spectra. In a time-independent atmosphere, H is thought to be ionized by a two-stage process: first, the n = 2 level is excited by electron collisions (which is very sensitive to the local temperature) and also by repopulation by scattered H Ly α photons in the massively opaque atmosphere, and second, the n=2 level is then photoionized by the optically thin photospheric Balmer continuum (Hartmann & Avrett 1984). In the simulation, we arbitrarily added a small H ionization fraction in the model to create the emission shown in the blue spectrum. We note that gas that is periodically heated in shocks can be cool and over-ionized behind the shocks, which might provide the additional ionization need to create $H30\alpha$ emission. The clumpy nature of H30 α in Figure 2 compared with X30 α suggests that its line-forming process is relatively unstable. If Lorentzian wing broadening is a result of high electron densities, then the H30 α emission (and some of the X30 α) must come from tiny pockets of hydrogen-ionized plasma; otherwise, the entire radio flux spectrum and angular sizes would be discrepant by factors of many (Harper & Brown 2006).

In summary, a plausible radial distribution of hydrogen and electron densities and gas temperature in the extended atmosphere leads to reasonable $X30\alpha$ emission both on and off the stellar disk, confirming the identification of this emission. The presence of $H30\alpha$ emission is readily explained by the presence of hot, perhaps shocked, plasma within the atmosphere. Indeed small volumes of hot plasma within the extended cooler material is the source of the rich UV chromospheric emission spectrum.

5. Conclusions

We can confidently identify the observed emission lines around 232 GHz in the ALMA spectra of Betelgeuse as $H30\alpha$ and $X30\alpha$. Synthetic spectra computed from a semiempirical model atmosphere are in good agreement with the continuum and line observations considering the simple modeling assumptions adopted. Interesting velocity differences of a few kilometers per second between the peaks of observed and modeled profiles remain unexplained. Line shapes show wings consistent with Voigt rather than Gaussian profiles, and electron densities within the hotter chromosphere are consistent with collisional line broadening. In the future, RTLs could prove to be valuable new diagnostics of the extended atmospheres of RSGs.

Acknowledgments

Support for G.M.H. was provided by grant HST-GO-16256.001-A provided by Space Telescope Science Institute, which is operated by the Association of Universities for Research in Astronomy, Incorporated, under NASA contract NAS5-26555. P.K. acknowledges funding from the European Research Council (ERC) under the European Union's Horizon 2020 research and innovation program (project UniverScale, grant agreement 951549). L.D.M. is supported by an award from the National Science Foundation (AST-2107681). This paper makes use of the following ALMA data: ADS/JAO. ALMA#2022.A.00026.S. ALMA is a partnership of ESO (representing its member states), NSF (USA) and NINS (Japan), together with NRC (Canada), MOST and ASIAA (Taiwan), and KASI (Republic of Korea), in cooperation with the Republic of Chile. The Joint ALMA Observatory is operated by ESO, AUI/NRAO and NAOJ.

Facility: ALMA.

ORCID iDs

W. R. F. Dent https://orcid.org/0000-0002-2490-1079 G. M. Harper https://orcid.org/0000-0002-7042-4541 A. M. S. Richards https://orcid.org/0000-0002-3880-2450 P. Kervella https://orcid.org/0000-0003-0626-1749 L. D. Matthews https://orcid.org/0000-0002-3728-8082

References

```
Airapetian, V. S., Ofman, L., Robinson, R. D., Carpenter, K., & Davila, J.
  2000, ApJ, 528, 965
Arroyo-Torres, B., Wittkowski, M., Chiavassa, A., et al. 2015, A&A, 575, A50
Asplund, M., Amarsi, A. M., & Grevesse, N. 2021, A&A, 653, A141
Aurière, M., Donati, J. F., Konstantinova-Antova, R., et al. 2010, A&A,
  516, L2
Brocklehurst, M., & Seaton, M. J. 1972, MNRAS, 157, 179
Carlsson, M., Rutten, R. J., & Shchukina, N. G. 1992, A&A, 253, 567
Carpenter, K. G., Nielsen, K. E., Kober, G. V., & Gioia, R. 2018, ApJ,
Carpenter, K. G., Robinson, R. D., Wahlgren, G. M., Linsky, J. L., &
  Brown, A. 1994, ApJ, 428, 329
Carr, J. S., Sellgren, K., & Balachandran, S. C. 2000, ApJ, 530, 307
CASA Team, Bean, B., Bhatnagar, S., et al. 2022, PASP, 134, 114501
Chang, E. S. 1987, PhyS, 35, 792
Chang, E. S., Avrett, E. H., Mauas, P. J., Noyes, R. W., & Loeser, R. 1991,
     pJL, 379, L79
De Beck, E., Vlemmings, W., Muller, S., et al. 2015, A&A, 580, A36
Decin, L. 2021, ARA&A, 59, 337
Gordon, M. A., & Sorochenko, R. L. 2002, Radio Recombination Lines. Their
  Physics and Astronomical Applications, Vol. 282 (Dordrecht: Kluwer)
Gustafsson, B., Edvardsson, B., Eriksson, K., et al. 2008, A&A, 486, 951
Harper, G. M., & Brown, A. 2006, ApJ, 646, 1179
Harper, G. M., Brown, A., Guinan, E. F., et al. 2017a, AJ, 154, 11
Harper, G. M., Brown, A., & Lim, J. 2001, ApJ, 551, 1073
Harper, G. M., DeWitt, C., Richter, M. J., et al. 2017b, ApJ, 836, 22
Harper, G. M., Guinan, E. F., Wasatonic, R., & Ryde, N. 2020, ApJ,
Harper, G. M., Richter, M. J., Ryde, N., et al. 2009, ApJ, 701, 1464
Hartmann, L., & Avrett, E. H. 1984, ApJ, 284, 238
Haubois, X., Perrin, G., Lacour, S., et al. 2009, A&A, 508, 923
Humphreys, R. M., & Jones, T. J. 2022, AJ, 163, 103
Jadlovský, D., Granzer, T., Weber, M., et al. 2023, arXiv:2312.02816
Judge, P. G. 1986, MNRAS, 221, 119
Judge, P. G., & Carpenter, K. G. 1998, ApJ, 494, 828
Kervella, P., Decin, L., Richards, A. M. S., et al. 2018, A&A, 609, A67
Lambert, D. L., Brown, J. A., Hinkle, K. H., & Johnson, H. R. 1984, ApJ,
  284, 223
```

Lim, J., Carilli, C. L., White, S. M., Beasley, A. J., & Marson, R. G. 1998,

Montargès, M., Cannon, E., Lagadec, E., et al. 2021, Natur, 594, 365

Montargès, M., Kervella, P., Perrin, G., et al. 2014, A&A, 572, A17
O'Gorman, E., Harper, G. M., Ohnaka, K., et al. 2020, A&A, 638, A65
Ohnaka, K. 2014, A&A, 561, A47
Ohnaka, K., Weigelt, G., Millour, F., et al. 2011, A&A, 529, A163
Olofsson, H., Black, J. H., Khouri, T., et al. 2021, A&A, 651, A35
Perrin, G., Verhoelst, T., Ridgway, S. T., et al. 2007, A&A, 474, 599
Richards, A. M. S., Davis, R. J., Decin, L., et al. 2013, MNRAS, 432, L61

Sundqvist, J. O., Ryde, N., Harper, G. M., Kruger, A., & Richter, M. J. 2008, A&A, 486, 985

Towle, J. P., Feldman, P. A., & Watson, J. K. G. 1996, ApJS, 107, 747
Uitenbroek, H., & Noyes, R. W. 1996, in ASP Conf. Ser. 109, Cool Stars, Stellar Systems, and the Sun, ed. R. Pallavicini & A. K. Dupree (San Francisco, CA: ASP), 723

Verhoelst, T., van der Zypen, N., Hony, S., et al. 2009, A&A, 498, 127 Wheeler, J. C., & Chatzopoulos, E. 2023, A&G, 64, 3.11